ReGeo ISSN: 2177-3246

PRODUCTION OF MIXED ZEOLITE USING AMAZONIAN NATURAL RESOURCES AND ITS APPLICATION IN THE REMOVAL OF LEAD FROM AQUEOUS SOLUTION

OBTENÇÃO DE ZEOLITA MISTA UTILIZANDO DE RECURSOS NATURAIS AMAZÔNICOS E SUA APLICAÇÃO NA REMOÇÃO DE CHUMBO DO MEIO AQUOSO

OBTENCIÓN DE ZEOLITA MIXTA A PARTIR DE RECURSOS NATURALES AMAZÓNICOS Y SU APLICACIÓN EN LA REMOCIÓN DE PLOMO DE MEDIOS ACUOSOS

10.56238/revgeov16n5-286

Ygor Geann dos Santos Leite[1], Francisco Xavier Nobre[2], Paulo Rogério da Costa Couceiro[3], João Paulo Ferreira Rufino[4], Milena Gaion Malosso[5], Rosany Picolotto Carvalho[6]

ABSTRACT

The search for sustainable approaches, particularly synthesis routes that typically involve long reaction times, high temperatures, and reagents derived from non-renewable sources such as petroleum, has been widely explored in recent decades. Accordingly, the results obtained in this study demonstrate that biogenic silica extraction from Amazonian Cauxi was successfully achieved, yielding a predominantly amorphous material with only trace amounts of crystalline quartz. Elemental analysis by X-ray fluorescence indicated silicon as the major component (82.43%), accompanied by minor amounts of aluminum (7.17%), phosphorus (0.76%), sulfur (0.72%), potassium (0.34%), calcium (0.46%), and titanium (0.062%). The transformation of kaolinite into metakaolinite was achieved through thermal treatment at 700 °C for 4 hours, confirmed by both X-ray diffraction and infrared spectroscopy, revealing the loss of kaolinite's characteristic crystallographic planes and the formation of an amorphous structural pattern, with residual peaks of quartz and anatase. Hydrothermal synthesis produced a multiphase zeolite mixture, consisting of Analcime (cubic, Ia-3d) and Pitiglianoite (hexagonal, P63), with crystallite sizes of 43 and 37 nm, respectively. Electron microscopy revealed spherical and porous microcrystals corresponding to Analcime, while elongated, rod-shaped crystals were attributed to Pitiglianoite. The elemental composition of the matrix, containing O, Na, Si, and Al, confirmed consistency with the expected formula. Porosity

[1] Doutorando em Biotecnologia. Universidade Federal do Amazonas. E-mail: ygor.geann.leite@gmail.com
[2] Doutor em Química. Instituto Federal de Educação, Ciência e Tecnologia do Amazonas.
E-mail: francisco.nobre@ifam.edu.br
[3] Doutor em Química. Universidade Federal do Amazonas. E-mail: couceiro35@gmail.com
[4] Doutor em Biodiversidade e Biotecnologia.
Instituto de Ciências Biológicas (ICB) da Universidade Federal do Amazonas.
E-mail: joao.rufino@ufam.edu.br
[5] Doutora em Biotecnologia. Instituto de Saúde e Biotecnologia (ISB) da Universidade Federal do Amazonas.
E-mail: milena@ufam.edu.br
[6] Doutora em Ciências da Saúde.
Instituto de Ciências Biológicas (ICB) da Universidade Federal do Amazonas.
E-mail: rosany.carvalho@ufam.edu.br

analysis via N_2 adsorption indicated a predominantly mesoporous structure, with a specific surface area of 11.433 $m^2\ g^{-1}$ (BET). Pb^{2+} adsorption tests demonstrated high capacity, reaching 77.23 mg g^{-1}, surpassing previously reported values in the literature. These results indicate that the combination of biogenic silica and alternative aluminum sources enables the production of multiphase zeolites with enhanced physicochemical properties, representing a promising strategy for heavy metal remediation in aqueous solutions.

Keywords: Zeolite. Analcime. Pitiglianite. Heavy Metals.

RESUMO

A busca por abordagens sustentáveis, principalmente as rotas de síntese que utilizam de longos períodos reacionais, elevadas temperaturas e reagentes oriundos de matriz não renovável como o petróleo, tem sido amplamente investigada nas últimas décadas. Desta forma, os resultados obtidos neste estudo indicam que a extração de sílica biogênica a partir do Cauxi amazônico foi realizada com sucesso, resultando em um material predominantemente amorfo, contendo apenas vestígios de quartzo cristalino. A análise elementar por fluorescência de raios X evidenciou que o silício é o principal componente (82,43%), acompanhado por pequenas quantidades de alumínio (7,17%), fósforo (0,76%), enxofre (0,72%), potássio (0,34%), cálcio (0,46%) e titânio (0,062%). A transformação da caulinita em metacaulinita foi obtida por tratamento térmico a 700 °C durante 4 horas, confirmada tanto por difração de raios X quanto por espectroscopia no infravermelho, evidenciando a perda dos planos cristalográficos característicos da caulinita e a formação de um padrão estrutural amorfo, com picos residuais de quartzo e anatase. A síntese hidrotérmica resultou em uma mistura multifásica de zeólitas, composta por Analcime (cúbica, Ia-3d) e Pitiglianoite (hexagonal, P63), apresentando tamanhos de cristalito de 43 e 37 nm, respectivamente. A microscopia eletrônica revelou microcristais esféricos e porosos correspondentes à Analcime, enquanto cristais alongados em formato de bastonete foram atribuídos à Pitiglianoite. A composição elementar da matriz, contendo O, Na, Si e Al, confirmou a conformidade com a fórmula esperada. O estudo de porosidade através da adsorção de N_2 indicou predominância mesoporosa, com área superficial específica de 11,433 $m^2\ g^{-1}$ (BET). Ensaios de adsorção de Pb^{2+} demonstraram elevada capacidade, alcançando 77,23 mg g^{-1}, superior a valores previamente reportados na literatura. Esses resultados mostram que a combinação de sílica biogênica e fontes alternativas de alumínio possibilita a obtenção de zeólitas multifásicas com propriedades físico-químicas aprimoradas, configurando uma estratégia promissora para remediação de metais pesados em soluções aquosas.

Palavras-chave: Zeólita. Analcime. Pitiglianoite. Metais Pesados.

RESUMEN

La búsqueda de enfoques sostenibles, en particular las rutas de síntesis que suelen implicar largos tiempos de reacción, altas temperaturas y reactivos derivados de fuentes no renovables como el petróleo, se ha explorado ampliamente en las últimas décadas. En consecuencia, los resultados obtenidos en este estudio demuestran que la extracción de sílice biogénica del Cauxi amazónico se logró con éxito, produciendo un material predominantemente amorfo con solo trazas de cuarzo cristalino. El análisis elemental por fluorescencia de rayos X indicó silicio como el componente mayoritario (82,43%), acompañado de cantidades menores de aluminio (7,17%), fósforo (0,76%), azufre (0,72%), potasio (0,34%), calcio (0,46%) y titanio (0,062%). La transformación de la caolinita en metacaolinita se logró mediante un tratamiento térmico a 700 °C durante 4 horas, confirmado tanto por difracción de rayos X como por espectroscopia infrarroja, revelando la pérdida de los planos cristalográficos característicos de la caolinita y la formación de un patrón

estructural amorfo, con picos residuales de cuarzo y anatasa. La síntesis hidrotermal produjo una mezcla de zeolita multifásica, compuesta por analcima (cúbica, Ia-3d) y pitiglianoíta (hexagonal, P63), con tamaños de cristalito de 43 y 37 nm, respectivamente. La microscopía electrónica reveló microcristales esféricos y porosos correspondientes a la analcima, mientras que los cristales alargados con forma de bastón se atribuyeron a la pitiglianoíta. La composición elemental de la matriz, que contiene O, Na, Si y Al, confirmó la consistencia con la fórmula esperada. El análisis de porosidad mediante adsorción de N_2 indicó una estructura predominantemente mesoporosa, con un área superficial específica de 11,433 m^2 g^{-1} (BET). Las pruebas de adsorción de Pb^{2+} demostraron una alta capacidad, alcanzando 77,23 mg g^{-1}, superando los valores reportados previamente en la literatura. Estos resultados indican que la combinación de sílice biogénica y fuentes alternativas de aluminio permite la producción de zeolitas multifásicas con propiedades fisicoquímicas mejoradas, lo que representa una estrategia prometedora para la remediación de metales pesados en soluciones acuosas.

Palabras clave: Zeolita. Analcima. Pitiglianita. Metales Pesados.

1 INTRODUCTION

Along the past decades, human activities have become the subject of intense reflection by the global scientific community, particularly regarding the future of species. Discussions have focused mainly on the environmental impacts resulting from these actions and on concerns about the possible depletion of natural resources, raising alarming predictions for future generations (HSIEH; YEH, 2024). In this context, various substances with toxic, carcinogenic, mutagenic, and highly persistent potential have become increasingly common in food, beverages, water, soil, and air. These contaminants are not restricted to urban areas, as they can be easily transported to different regions of the planet, especially through bodies of water, both surface and groundwater (MICHELANGELI *et al.*, 2022; RAMAN *et al.*, 2024).

The contamination of water resources by heavy metals, particularly lead (Pb) and cadmium (Cd), constitutes an environmental problem of global scale, with serious repercussions for public health, especially in urban regions with intense industrial activity (AFZAL *et al.*, 2024). Due to this issue, there has been a significant increase in scientific production aimed at improving technologies and methodologies for the detection, monitoring, and remediation of potentially toxic chemical species. This trend reflects international recognition of the seriousness of the matter and its strategic relevance for public health institutions and agencies worldwide (SARAVANAN *et al.*, 2024; SULTHANA *et al.*, 2024). In this scenario, contemporary epidemiological investigations have shown that prolonged exposure to heavy metals, even at trace levels, is correlated with severe and irreversible adverse effects on the nervous system, kidneys, and cardiovascular system (JOMOVA *et al.*, 2025; KHELIFI *et al.*, 2021). Given this situation, advancing technological remediation approaches that combine efficiency and sustainability becomes imperative, enabling their application in diverse contexts while considering the socioeconomic and environmental particularities of each region.

Despite the widespread use of conventional methods, such as adsorption on activated carbon, ion exchange with resins, and reverse osmosis systems, these techniques present significant limitations related both to the performance of the materials employed and to operational costs. Such constraints have driven the search for new technological pathways and alternative materials that are more efficient and economically viable for the removal of heavy metals from effluents (XU *et al.*, 2024). In the contemporary context of environmental remediation technologies, zeolites have been increasingly recognized as materials with great potential for heavy metal removal, owing to their highly porous crystalline framework, large specific surface area, and remarkable efficiency in ion-exchange processes (ABDELHALIM;

MELEGY; OTHMAN, 2025; KHALEQUE *et al.*, 2020; SILVA FILHO *et al.*, 2015). However, traditional zeolite synthesis routes present important restrictions, such as high energy consumption and the requirement for costly synthetic reagents. In response to these limitations, an alternative and still relatively unexplored strategy has emerged, centered on the controlled generation of multiphasic systems in which distinct zeolitic structures coexist and establish synergistic interactions that can enhance material performance (PÉREZ-BOTELLA; VALENCIA; REY, 2022). This strategy offers distinct advantages in terms of efficiency and versatility, as demonstrated in recent studies (QI *et al.*, 2016).

Aligned with the principles of the circular economy and the strengthening of the bioeconomy, the rational and innovative use of Amazonian natural resources as sustainable substitutes for non-renewable synthetic reagents emerges as a promising strategy. This approach not only highlights the scientific and technological potential of the region but also contributes to the qualified training of professionals and to the development of technologies with national identity and value (ARAUJO *et al.*, 2024). In the study conducted by Barros *et al.*, (2020) the authors report the production of heterogeneous solid catalysts from residual biomass of pineapple leaves sourced from the community of Novo Remanso in Amazonas, which resulted in high-performance conversion of vegetable oil into biofuel In another study developed by Soares *et al.*, (2022), Amazonian metakaolin, obtained from the thermal treatment of the mineral kaolinite, was used in the preparation of cementitious boards mixed with residual plastic, as an ecologically viable proposal for the development of artifacts for acoustic insulation. Meanwhile, in studies conducted by Silva Filho *et al.*, (2015) the authors report the synthesis of the zeolites Analcime and Zeolite A using Amazonian metakaolin as a source of silicon and aluminum, adopting the hydrothermal method at temperatures between 100 and 220 °C.

Thus, the production of zeolites from natural inputs or residual materials represents a less environmentally impacting alternative, in addition to offering economic and ecological feasibility. This strategy has become an innovative trend in obtaining materials whose properties and characteristics are comparable to those of zeolites synthesized by conventional pathways (KHALEQUE *et al.*, 2020). In line with this perspective and considering the use of regional natural resources, the promising potential for obtaining biogenic silica, namely, silicon dioxide (SiO_2), from the Amazonian Cauxi sponge (*Metania kiliani*) stands out (LACERDA; COUCEIRO, 2019). This species, popularly known as the Amazonian freshwater sponge, is widely distributed in rivers across the region and is noteworthy for its abundance, ease of processing, and high degree of purity in its inorganic fraction (SOUSA *et al.*, 2025).

On the other hand, the mineral potential of the Amazon region, especially kaolin ($Al_2Si_2O_5(OH)_4$), offers an accessible and still underexplored source of silicon oxide and aluminum oxide for technological applications (PRUETT, 2016). The combination of these precursors enables the synthesis of zeolitic materials with unique properties, whose structural complexity broadens their potential applications in various fields, including water and gas purification processes (ABDELHALIM *et al*., 2025), catalysis (PALA-ROSAS *et al.*, 2023), antimicrobial agents (DE LEÓN RAMIREZ *et al.*, 2024), luminescent materials (LIU *et al.*, 2024), and heavy metal adsorption (VELARDE *et al.*, 2023),

Based on the above, the present study sought to explore an alternative route for zeolite production, adopting the hydrothermal method using Amazonian natural resources, specifically, biogenic silica obtained from the spicules of the Amazonian Cauxi sponge and metakaolinite derived from kaolinite clay. The synthesized zeolite was structurally characterized using different analytical techniques and its potential for the removal of lead ions from an aqueous medium was also investigated.

2 MATERIALS AND METHODS

2.1 MATERIALS

All reagents used in this study were employed without prior purification. Thus, nitric acid (HNO_3, Sigma-Aldrich, purity > 65%), hydrogen peroxide (H_2O_2, Synth, 30 volumes, analytical grade-PA), , and hydrochloric acid (HCl, Merk, purity > 27%) were acquired directly from the manufacturers based in São Paulo, Brazil.

2.2 PREPARATION OF BIOGENIC SILICA FROM THE AMAZONIAN FRESHWATER SPONGE

Samples of Cauxi were collected near the ruins of the former Ariaú Hotel, located on the banks of the Negro River, in the municipality of Iranduba, state of Amazonas. The collection site was georeferenced at 3°5'29.630" S and 60°26'25.559" W.

The extraction of biogenic silica began with natural drying of the samples for 48 hours at room temperature to ensure complete removal of residual moisture. After drying, the material was carefully fragmented until obtaining fine spicules suitable for subsequent chemical treatment. Exactly 20 grams of the crushed Cauxi were weighed and subjected to an oxidizing solution composed of hydrogen peroxide (H_2O_2), nitric acid (HNO_3), and distilled water at a volumetric ratio of 8:7:1. The mixture was kept under controlled heating at 90 °C for 20 minutes to ensure efficient oxidation of the organic matter.

After the reaction, the resulting material was filtered through a porcelain funnel, and the oxidation–filtration cycle was repeated successively until the residue displayed a whitish coloration, indicating full purification. Finally, the sample was dried at 160 °C for 2 hours, yielding the final product, purified biogenic silica. Figure 1 presents a schematic representation of the steps involved in the extraction of biogenic silica from Cauxi.

Figure 1

Schematic representation of the extraction and purification steps of biogenic silica from Cauxi.

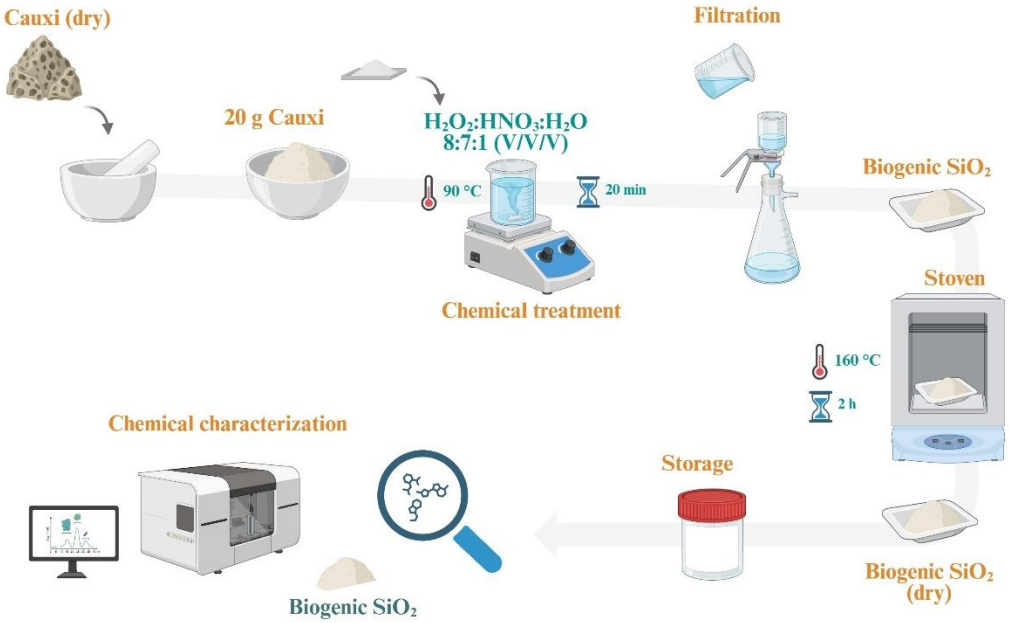

2.3 PRODUCTION OF METAKAOLINITE FROM AMAZONIAN KAOLIN

A sample of Amazonian soil with a high kaolinite content was collected at kilometer 45 of highway BR-174, on the Manaus-Boa Vista route, near the bridge over the Cabeça Branca stream, located at coordinates 2°35'9.802" S and 60°1'58.566" W. Approximately 500 grams of this material were manually disaggregated and air-dried for 48 hours, producing what was designated air-dry soil. The material was then subjected to granulometric separation using a 0.063 mm mesh sieve; the retained fraction was discarded, and the passing fraction, referred to as the sieved fine fraction (FFP), was used for subsequent purification steps.

The FFP underwent chemical treatment in a 10% (v/v) hydrochloric acid solution under continuous stirring and controlled heating. After treatment, the material was filtered and washed repeatedly with distilled water until reaching neutral pH. The resulting sample was dried in an oven at 100 °C for 24 hours, yielding the acid-treated fine fraction, characterized by greater physicochemical uniformity. In the next step, the material was calcined in a muffle furnace at 700 °C for 4 hours, followed by gradual cooling in a desiccator.

2.4 SYNTHESIS OF ZEOLITE USING AMAZONIAN PRECURSORS

The synthesis of the zeolite began with the preparation of two solutions, referred to as solution A and solution B. For solution A, 3.81 g of metakaolinite were mixed with 0.585 g of sodium hydroxide in 10 mL of distilled water in a 50 mL plastic beaker. Solution B was prepared by mixing 3.84 g of biogenic silica from Cauxi with 0.585 g of sodium hydroxide and 10 mL of distilled water in a similar beaker. Both mixtures were subjected to magnetic stirring until complete dissolution of the solid components, resulting in the formation of a precursor gel.

The crystallization step was performed at 120 °C for 36 hours in an oven. Before heating, the suspension obtained in the previous step was transferred to a 100 mL Teflon reactor vessel and maintained under constant magnetic stirring. After crystallization, the material was collected by centrifugation, washed several times with distilled water until the pH reached approximately 8, and subjected to centrifugation cycles at 6000 rpm for 5 minutes. The schematic diagram shown in Figure 2 summarizes the steps used for zeolite synthesis via the hydrothermal method.

Figure 2

Schematic representation of the steps used in the synthesis of zeolite from Amazonian raw materials.

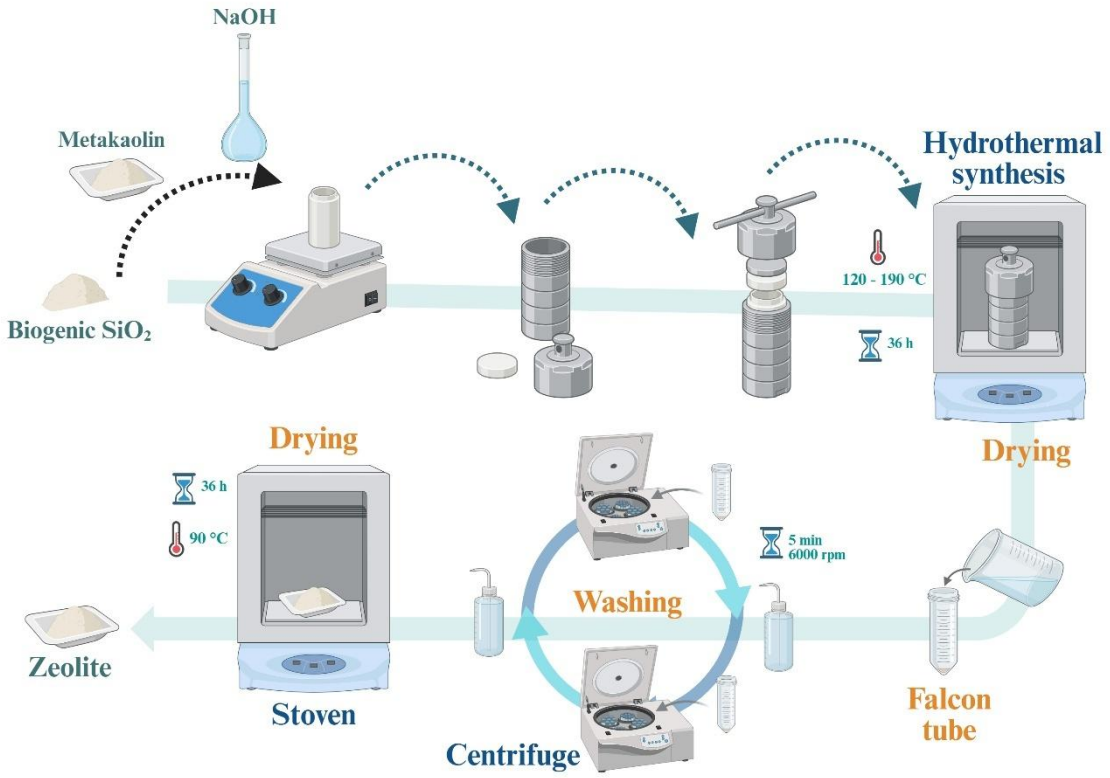

2.5 CHARACTERIZATION TECHNIQUES

2.5.1 X-ray Diffraction

Diffraction patterns were collected using the powder method on a Shimadzu XRD-7000 diffractometer equipped with a copper anode X-ray source (CuKα radiation, λ = 0.15406 nm). Crystallographic information was recorded over a 2θ range of 10°–100° with a step of 0.02° min^{-1}. Structural refinement was carried out using the Rietveld method with the FullProf software package, October 2025 Windows version.

2.5.2 Infrared Vibrational Spectroscopy

Vibrational spectra of the prepared samples were collected using an Agilent Cary 630 FTIR spectrometer equipped with a zinc selenide (ZnSe) crystal. Thirty-two scans per sample were acquired in Attenuated Total Reflectance (ATR) mode with a resolution of 4 cm^{-1} and a spectral range of 650-4000 cm^{-1}.

2.5.3 Scanning Electron Microscopy (SEM) and Energy-Dispersive X-ray Spectroscopy

Morphological analysis and particle size information were obtained using a FEI Quanta FEG 250 scanning electron microscope. Images were acquired at an accelerating voltage of 10 kV (operational range 1–30 kV). For sample preparation, 20 mg of material were dispersed in 1 mL of acetone and submitted to ultrasonic agitation for 3 minutes. Then, 100 µL of the suspension were pipetted onto carbon tape adhered to an aluminum stub. Samples were gold-coated via sputtering using a Quorum Q150R ES coater. SEM micrographs were acquired using both secondary electron (SE) and backscattered electron (BE) detectors.

2.5.4 X-ray Fluorescence Spectroscopy

Semiquantitative analysis was performed using a Malvern Panalytical EPSON 4 spectrometer equipped with a high-resolution (135 eV) silicon drift detector (SDD) and Mn-Kα radiation. The loose powder method was used for this study. The assay was conducted in triplicate, placing approximately 5 g of sample into a polyethylene cup sealed at one end with a Mylar polymer membrane (polyethylene/Kapton).

2.5.5 Atomic Absorption Spectroscopy

Quantitative analysis of lead-containing solutions for calibration curve construction, as well as post-adsorption solutions, was performed using a Thermo Scientific iCE 3000 SERIES atomic absorption spectrometer equipped with an HGA 800 graphite furnace. Background correction was carried out using a deuterium lamp, and high-purity argon (99.99%) was used

as the purge gas. A lead hollow-cathode lamp was used at 283.3 nm with a spectral bandwidth of 2.7/1.05 nm and a current of 10 mA. Lead standard solutions used for calibration were prepared at concentrations of 0.25 ppm, 0.50 ppm, 0.75 ppm, 1.00 ppm, and 1.50 ppm.

3 RESULTS AND DISCUSSION

The semiquantitative analysis was conducted to determine the elemental composition of the biogenic silica (B-SiO_2) obtained from the chemical treatment of Cauxi spicules, with particular attention to the detection of trace elements commonly found in biologically derived matrices. As illustrated in Figure 3, silicon is the predominant element in the sample, appearing at a concentration markedly higher than all other chemical species, with a percentage value of 82.427%. In smaller proportions, aluminum (7.174%), phosphorus (0.76%), sulfur (0.715%), potassium (0.339%), calcium (0.457%), and titanium (0.62%) were identified. These results confirm the predominance of the silicate matrix and the residual presence of impurities typical of natural precursors.

These findings are in accordance with the study conducted by De Barros (2014), who investigated the composition of *Drulia browni* sponges collected in the Negro River, Amazonas, and reported silicon, aluminum, and calcium as the elements present in highest concentrations i.e., above 3%, while sulfur, potassium, and iron were observed at concentrations below 3%. In the same study, the authors also analyzed specimens of Metania fittkaui Volkmer-Ribeiro collected from distinct regions of the Amazon basin, namely the Mapi stream in the municipality of São Gabriel da Cachoeira, and specimens collected in Lago do Encanto, on the Tapajós River, in the municipality of Belterra, Pará. In both cases, the species exhibited a major elemental composition dominated by silicon (Si = 42.30% ± 2.69%), while the minor elements, sulfur, vanadium (V), iron, and copper, were present at concentrations below 1%. When compared with the present study, it is suspected that the percentage reported for vanadium in the aforementioned work may, in fact, correspond to titanium, since these two elements have closely similar Kα and Kβ emission energies, and titanium is more commonly reported in the literature on soils and waters of the Amazon basin than vanadium (MARUOKA *et al.*, 2023).

Figure 3

(a) X-ray diffraction pattern and (b) X-ray fluorescence spectrum of the biogenic SiO_2 (B-SiO_2).

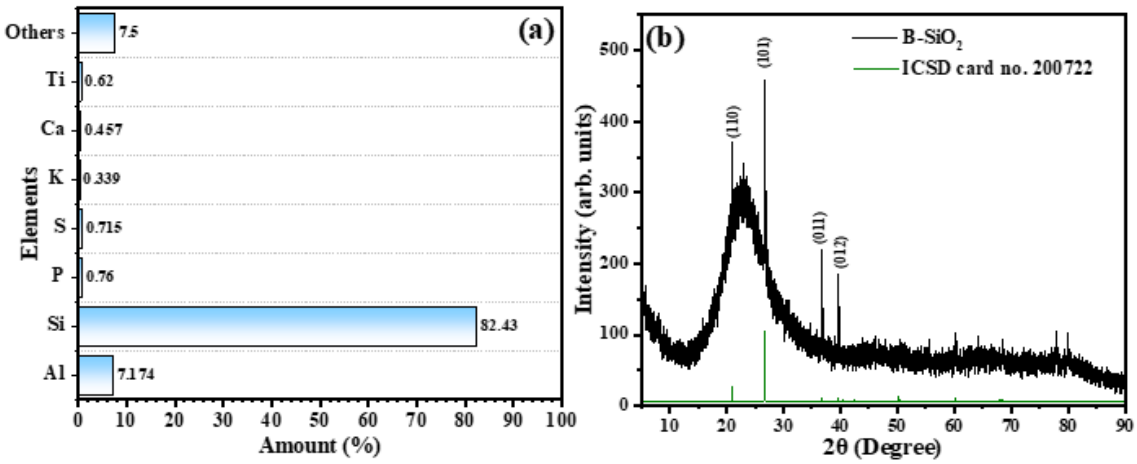

The analysis of the diffractogram of the biogenic silica (B-SiO_2) sample, illustrated in Figure 3(b), shows, according to the performed indexing, that the material exhibits a predominantly amorphous silicon oxide structure. This characteristic is confirmed by the typical diffractometric profile of substances with a low degree of structural ordering, marked by the presence of a broad diffuse halo centered at 2θ = 23.1°, which corroborates the non-crystalline nature of the sample and supports the experimental observations (SOARES *et al.*, 2022). In addition, crystallographic planes corresponding to diffraction angles at 2θ = 21.03°, 26.84°, 36.82°, and 39.78° were identified, typical of silicon oxide phases with a high degree of crystallinity. These reflections confirm the presence of quartz in the sample, whose crystalline structure is trigonal and belongs to the $P3_121$ space group (No. 152), containing three formula units per unit cell (Z = 3). The observed match shows strong agreement with the crystallographic pattern described in the ICSD database under entry No. 20072 (JORGENSEN, 1978) and with consulted literature (PAVAN *et al.*, 2023).

Structural analysis was likewise performed for the Amazonian kaolin samples, both in their natural form and after thermal treatment, to elucidate the structural transformations induced by the process. This characterization served as a complementary tool in verifying the conversion of the kaolinite phase into metakaolinite, resulting from the disruption of the original three-dimensional network, as partially illustrated in Figure 4(a–b) (ANDRADES *et al.*, 2020; GUZMÁN-APONTE; DE GUTIÉRREZ; MAURY-RAMÍREZ, 2017; SOARES *et al.*, 2022).

As illustrated in Figure 4(a), the diffractogram obtained for kaolinite after undergoing the physical and chemical treatments exhibits the characteristic behavior of materials with a

high degree of structural ordering over both short and long ranges. The physical treatment, based on sieving, promoted the predominant separation of fractions composed of crystalline silica grains, while the chemical stage, conducted with strong acids, particularly nitric acid, responsible for leaching iron and other structural impurities, resulted in a diffraction pattern consistent with a highly organized and crystalline structure.

The diffraction analysis, combined with the indexing of crystallographic planes corresponding to peaks in the 2θ range between 10° and 80°, revealed that the sample predominantly exhibits a triclinic phase belonging to the P1(1) space group. The identified structure is consistent with the chemical formula $Al_2(Si_2O_5)(OH)_4$, with lattice parameters determined as a = 5.158 Å, b = 8.942 Å, and c = 7.397 Å, and interaxial angles of α = 91.672°, β = 104.860°, and γ = 89.898°. These results show remarkable agreement with the crystallographic data reported in reference card No. 20593, reinforcing the structural consistency of the observed phase (EL-SAYED; HEIBA; ABDEL-RAHMAN, 1990) and consulted literature (CECILIA *et al.*, 2022; CHAKRABORTY, 2014; CHENG; ZHOU; LIU, 2019; EL-SAYED; HEIBA; ABDEL-RAHMAN, 1990). In addition to the crystallographic planes assigned to the kaolinite phase, additional reflections were observed indicating a residual fraction of silicon dioxide in its crystalline form (quartz). The correspondence of these diffractive peaks presents high agreement with the crystallographic data reported in ICSD entry No. 200722, corroborating the coexistence of this secondary phase in the analyzed material.

Figure 4

(a) diffraction pattern of the kaolinite sample and theoretical diffraction pattern of kaolinite and quartz structures, and (b) diffraction pattern of the metakaolinite sample and theoretical diffraction pattern for the quartz and anatase (TiO_2) structures.

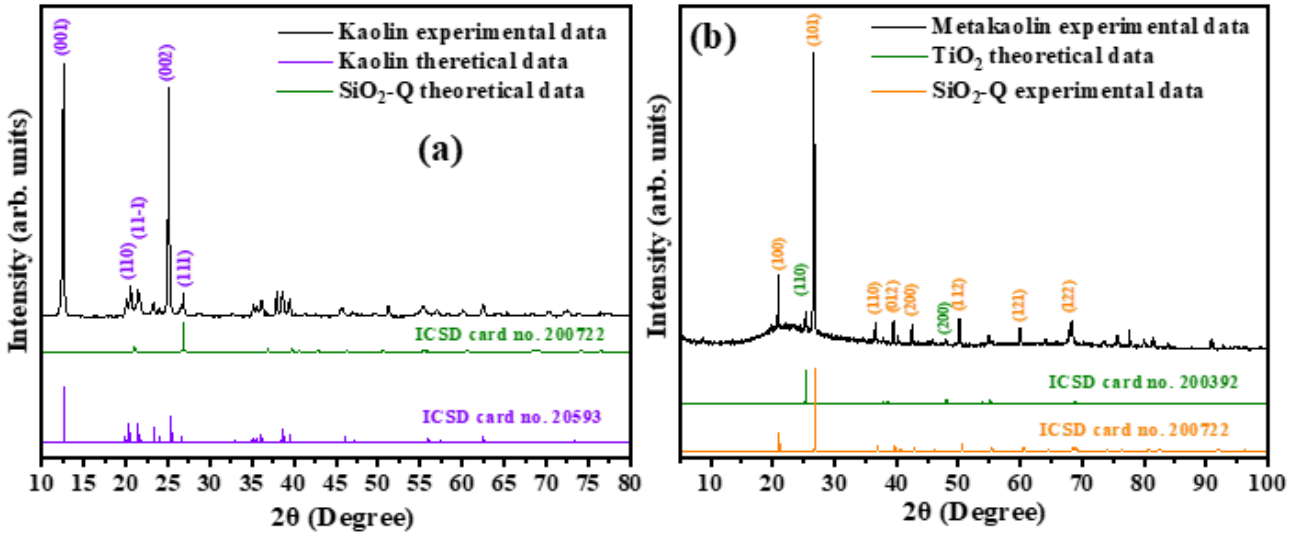

The structural conversion of kaolinite into its dehydroxylated form, metakaolinite, was evidenced by the change in the XRD profile shown in Figure 4(b), corresponding to the sample subjected to 700 °C for 4 hours under an uncontrolled atmosphere. The diffractogram reveals the predominance of reflections typical of the trigonal quartz lattice, identified by the crystallographic planes (100), (101), (110), (012), (200), (112), (121), and (122), as previously discussed. In addition, additional peaks assigned to the tetragonal anatase phase of titanium dioxide (TiO_2), belonging to the $I4_1/amd$ (141) space group, were recorded, with its most intense diffraction maxima located at 2θ = 25.47° and 47.93°, corresponding to the (110) and (200) planes. These results exhibit excellent agreement with the crystallographic information reported in ICSD card No. 200392, as well as with data published in related scientific literature (ALBUQUERQUE *et al.*, 2015; MI *et al.*, 1998; WANG *et al.*, 2007).

In the angular range between 10° and 40° (2θ), a diffuse pattern characteristic of amorphous materials is observed, although the crystallographic planes previously identified for the aforementioned phases remain perceptible. This behavior highlights the structural disorder resulting from the dissociation of the silicon [SiO_4] and aluminum [AlO_4] tetrahedra, caused by the rupture of hydroxyl-mediated bonds and metal–oxygen–metal bridges during the heating process. This effect, widely documented in classical studies on the dehydroxylation of kaolinite and its conversion into metakaolinite under similar thermal conditions, corroborates the efficiency of the treatment adopted and confirms the successful formation of the intended material.

To verify the loss of the structural ordering characteristic of kaolinite following thermal treatment, morphological analysis was performed by scanning electron microscopy (SEM), complemented by elemental mapping of the matrix, as partially shown in Figure 5(a-f). The micrograph in Figure 5(a) reveals the disordered rearrangement of the constituent particles of the metakaolinite sample, a behavior widely described in the specialized literature as indicative of structural transformation resulting from dehydroxylation and partial collapse of the crystalline framework (MARUOKA *et al.*, 2023). Initially, the material exhibits a highly organized pattern of hexagon-shaped platelets, which becomes tridimensionally disordered after thermal treatment, with an associated change in the thermogravimetric curve within the temperature range of 400–800 °C. The maximum transition process is observed at 463 °C, as reported in the study by Zuo *et al.*, (2022).

The evidence obtained consistently reinforces the results of the other analyses performed, particularly the X-ray diffraction data previously discussed. A clear presence and homogeneous distribution of the main elements constituting the matrix, silicon (Si), aluminum (Al), and oxygen (O), are observed, along with a residual fraction of titanium (Ti), as illustrated

in the elemental maps shown in Figures 5(b-e) and in the energy-dispersive X-ray (EDX) spectrum presented in Figure 5(f). Thus, the results consolidate the structural and compositional interpretations previously established for the analyzed sample.

Figure 5

Scanning electron microscopy of the sample: (a) metakaolinite with identification maps of the elements (b) oxygen, (c) aluminum, (d) silicon, and (e) titanium, while (f) corresponds to the EDX spectrum of the elements present in the matrix.

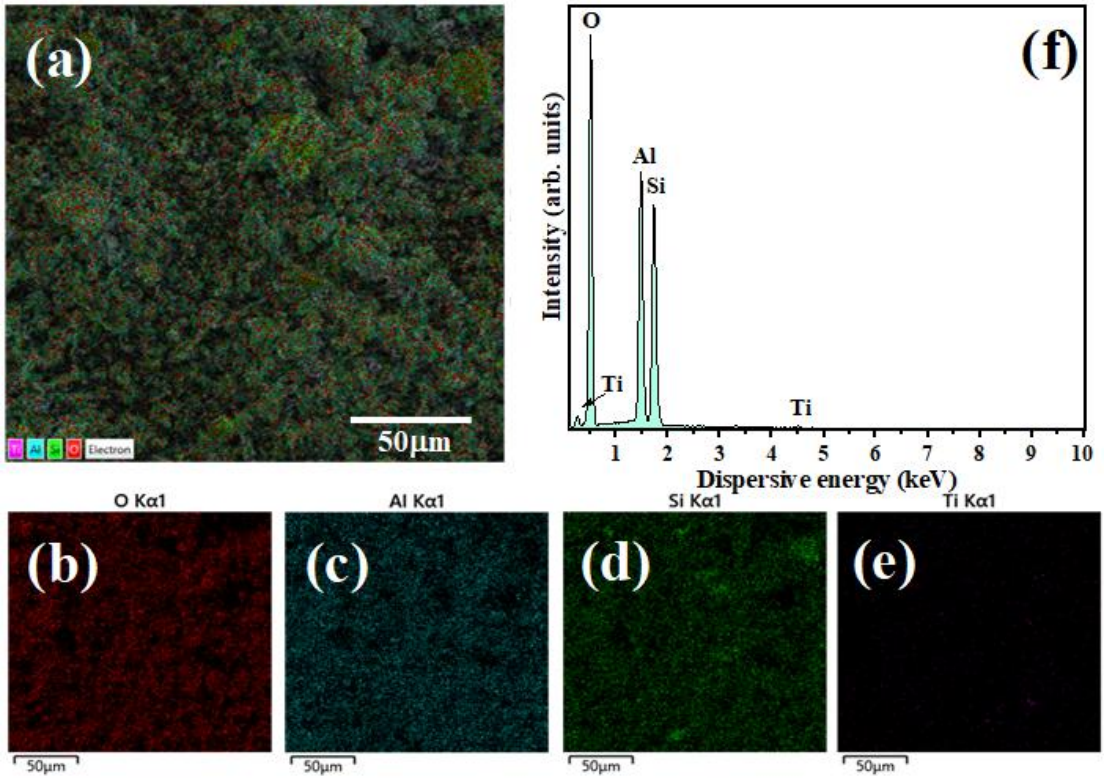

Additionally, Fourier-transform infrared vibrational spectroscopy (FTIR) was applied to identify changes in the characteristic bands of the kaolinite structure and to verify complementary evidence supporting the structural transformation proposed in this work. As illustrated in Figure 40, the vibrational spectrum of the kaolinite sample (represented by the black line) reveals nine distinct bands corresponding to molecular vibrations in the spectral region from 650 to 4000 cm^{-1}, specifically observed at 749 cm^{-1}, 790 cm^{-1}, 912 cm^{-1}, 998 cm^{-1}, 1035 cm^{-1}, 1118 cm^{-1}, 3620 cm^{-1}, 3652 cm^{-1}, and 3864 cm^{-1}. According to the consulted literature (MARIA, 2020), in the spectral region between 3500 and 4000 cm^{-1}, the symmetric stretching vibrational modes of O-H bonds are observed, corresponding to terminal hydroxyl groups located at the edges of the [AlO_4] and [SiO_4] tetrahedra. After thermal treatment, these bands are completely suppressed in the spectrum of the kaolinite

sample, indicating the elimination of hydroxyl groups through the release of water molecules, a phenomenon that precedes and confirms the onset of structural disorder in the material.

Figure 6

FTIR vibrational spectroscopy of kaolinite and metakaolinite.

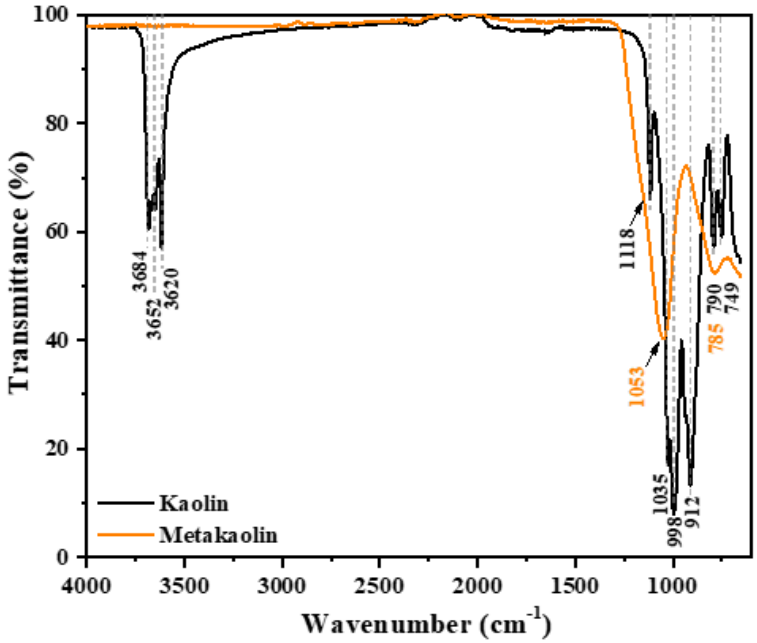

The moderately intense band observed at 1118 cm^{-1} is associated with the symmetric stretching modes of Si–O bonds, whereas the signal at 1035 cm^{-1} corresponds to the bending vibrations of Si–O–Si linkages. The bands located at 998 cm^{-1} and 912 cm^{-1} are typical of the kaolinite structure and are assigned, respectively, to the vibrations of Si-O-Al and Al-OH bonds, reflecting the integrity of the lamellar network characteristic of this mineral (EL-SAYED *et al.*, 1990). Finally, the bands at 749 cm^{-1} and 790 cm^{-1} correspond, according to the consulted literature, to Si-O stretching modes in crystalline silicon oxide structures, clear evidence of the presence of quartz, corroborating the interpretations previously discussed in the diffraction pattern of this sample(MARUOKA *et al.*, 2023).

After the calcination step, a significant alteration is observed in the bands within the 650–1200 cm^{-1} region, indicating substantial modifications to the material's structure. These spectral variations confirm the structural transformation previously discussed, evidencing the progressive disordering of the kaolinite crystalline framework and its effective conversion into metakaolinite (GAO *et al.*, 2020). Accordingly, only two broad, well-defined bands are observed in the spectra, located at 785 cm^{-1} and 1053 cm^{-1}. The 785 cm^{-1} band is related to the stretching vibrational modes of Si-O bonds characteristic of quartz, in agreement with the X-ray diffraction results. The band at 1053 cm^{-1} is attributed to the stretching vibrations of M-

O-M linkages, where the metal element M corresponds to aluminum or silicon present in the matrix (GAO *et al.*, 2020; KYRIAKOGONA *et al.*, 2017; MARIA, 2020).

Thus, the results confirm the successful conversion of kaolinite into its dehydroxylated form, metakaolinite. This structural transformation verifies the efficiency of the treatment applied and validates the use of the resulting material as a precursor in the subsequent zeolite synthesis steps, reinforcing its applicability as an alternative source of aluminum and silicon for zeolite production. The investigation of the structural properties of the zeolite obtained from the hydrothermal processing of metakaolin with biogenic silica from Cauxi was initially carried out by XRD, with the results graphically presented in Figure 7(a–b).

Figure 7

(a) Diffraction pattern of the synthesized zeolite and (b) structural refinement plot used for the identification and quantification of crystalline phases.

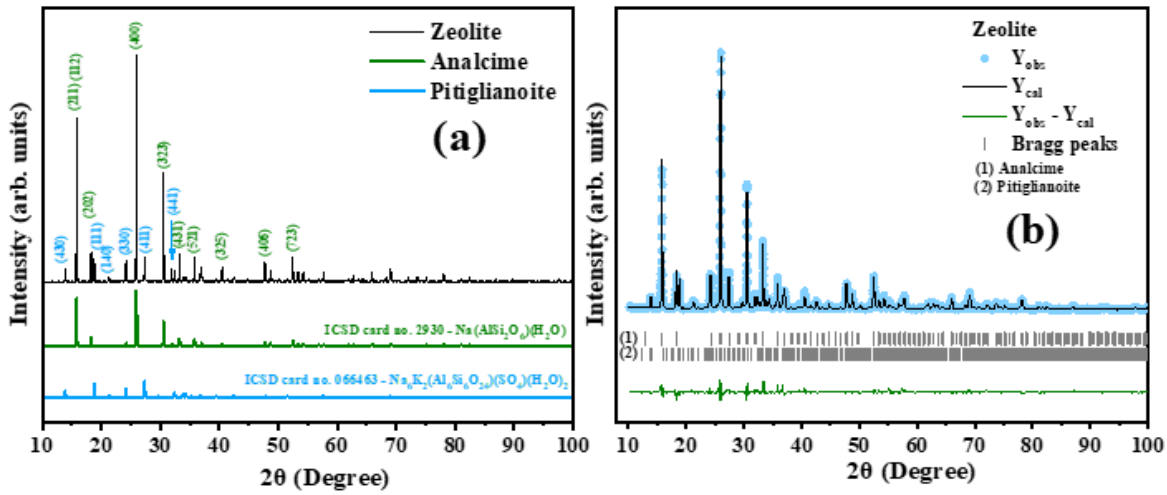

The analysis and indexing of the diffractogram shown in Figure 7(a) confirm that the synthesized sample is composed of a combination of crystalline phases, with the predominance of the zeolite Analcime. This material has the chemical formula $Na(AlSi_2O_6)\cdot H_2O$ and a cubic crystalline structure belonging to the Ia-3d space group. Its lattice parameters are equal (a = b = c = 13.7300 Å), resulting in a unit cell volume of 2588.28 Å³ and containing 24 formula units. The information obtained shows excellent agreement with the crystallographic data recorded in the ICSD database (No. 2930), as well as with patterns reported in specialized literature (MALLETTE *et al.*, 2024; MORAES *et al.*, 2013). Additionally, a second crystalline phase belonging to the hexagonal system was identified and indexed, corresponding to the zeolite Pitiglianoite. This structure belongs to the $P6_3$ space group and presents lattice parameters a = b = 22.1210 Å and c = 5.2210 Å, with a unit cell volume of 2212.55 Å³ containing three formula units (Z = 3). The obtained data show high

correspondence with the crystallographic information available in ICSD record No. 066463, and fully agree with previous studies describing this zeolitic phase, such as the report by Merlino *et al.*, (1991) on samples extracted from southern Tuscany, Italy.

The diffractogram obtained for the synthesized zeolite sample exhibits sharp, high-intensity peaks with minimal broadening. This behavior confirms that both crystalline phases display a remarkable degree of structural order, reflecting high crystallinity and consistent periodicity at both local and long-range scales (NOBRE *et al.*, 2019; NOBRE *et al.*, 2023). Such properties are characteristic of materials produced by hydrothermal synthesis, in which controlled temperature, and consequently the internal pressure of the reactor, promotes atomic rearrangement and the orderly growth of the crystalline lattice. This synthesis environment fosters a high degree of regularity in the arrangement of structural clusters, resulting in solids with notable crystallinity (RHODES, 2010).

In the early stages of synthesis, an intense electrostatic interaction occurs between the ions present in the reaction medium, amplified by the high concentration of hydroxyl groups typical of strongly alkaline environments. This condition favors the activation and self-organization of clusters that form the zeolite framework, in which Na^+ and K^+ cations play essential roles as counterions, contributing to charge balance as well as to the stabilization and proper tension of the resulting crystalline network (PÉREZ-BOTELLA *et al*., 2022). The sequence of reactivity, nucleation, growth, and self-assembly follows the principles of mesostructure formation governed by the Ostwald ripening mechanism (OUYANG; LIU; LI, 2013).

Additional crystallographic analyses were carried out through structural refinement using the Rietveld method, which integrates the experimental data obtained from the sample's diffractogram and the theoretical parameters derived from the crystallographic files of Analcime and Pitiglianoite (ICSD Nos. 2930 and 66463, respectively). Data processing and fitting were performed with the aid of the FullProf software package (October 2025 Windows version).

During refinement, priority was given to determining the proportions of the crystalline phases, atomic coordinates, lattice parameters, unit cell volumes, and background correction, using the Thompson–Cox–Hastings (TCH) pseudo-Voigt function to fit peak intensities and shapes. Refinement quality was evaluated using the R-agreement factors (Rp, Rwp, Rexp, and χ^2), as well as the residual line, defined as the difference between observed (Yobs) and calculated (Ycal) intensities. Following established criteria in the literature, refinements were considered satisfactory when $\chi^2 \leq 2$ or GoF < 2 for single-phase systems, and $\chi^2 \leq 5$ or GoF < 2.5 for multiphase systems (TOBY, 2006).

Based on the graphical results shown in Figure 7(b), along with the information in Table 1, it is evident that the computed calculations yielded excellent agreement between experimental and theoretical data. The reproducibility and reliability of the refined parameters are confirmed by the GoF value lower than 2. Furthermore, the residual line indicates minimal deviation between experimental intensities and the theoretical fit.

The structural refinement evidenced the simultaneous presence of the crystalline phases corresponding to Analcime and Pitiglianoite, whose relative proportions were estimated at 71.02 ± 0.54% and 28.98 ± 0.47%, respectively, confirming the predominance of the Analcime phase in the synthesized sample. For Analcime, the refined lattice parameters were a = b = 13.723(2) Å and c = 13.722(6) Å, resulting in a unit cell volume (V) of 2584.315(7) Å³, values in excellent agreement with the crystallographic data recorded in ICSD card No. 2930. Similarly, Pitiglianoite exhibited lattice parameters a = b = 22.067(1) Å and c = 5.214(3) Å, with a unit cell volume of 2198.955(3) Å³, also in full accordance with the structural information described in its reference file, reinforcing the precision and reliability of the refinement results.

The average crystallite size ($\overline{D}_{hkl}$) of the zeolitic phases in the synthesized material was calculated using the Scherrer method, following the mathematical formulation shown in Equation 1.

$$\overline{D}_{hkl} = \frac{k\lambda}{\beta_{tot} cos\theta} \quad (1)$$

In this equation, *k* corresponds to the constant associated with the shape factor. In this study, *k = 0.9* was adopted, which assumes an approximately spherical morphology for the particles. The parameter λ represents the wavelength of the radiation used by the diffractometer anode during acquisition of the diffraction pattern (CuKα = 0.15406 nm), and θ is the angle associated with each diffraction peak. In this study, the mean value of the main crystallographic planes of both phases was used, as provided in the output file generated after each refinement cycle. Finally, β_{tot} corresponds to the full width at half maximum (FWHM) of the diffraction peaks of the sample, obtained by correcting the sample broadening (β_{sample}) for instrumental contribution ($\beta_{instrumental}$). For this purpose, the diffraction pattern of lanthanum hexaboride (LaB_6, Sigma-Aldrich, purity > 99.99%) was refined. The correction equation used to calculate β_{tot} is presented in Equation 2.

$$\beta_{tot} = \sqrt{\beta_{sample}^{\ 2} - \beta_{instrumental}^{\ 2}} \quad (2)$$

Based on the methodology employed, the calculations revealed that the Analcime and Pitiglianoite zeolites exhibit average crystallite sizes of approximately 43 nm and 37 nm, respectively. These results demonstrate that both structures fall within the nanometric range, a characteristic that directly influences their textural and morphological properties. This, in turn, allows one to infer a high degree of structural refinement and a potentially enhanced performance in applications that depend on surface area and crystalline organization.

Table 1

Results obtained from the structural refinement of the zeolite sample using the Rietveld method, and crystallographic information from ICSD cards No. 2930 and No. 66463.

Parameters	Zeolite	Crystallographic information	
		ICSD card no. 2930	ICSD card no. 66463
Analcime			
a = *b* (Å)	13.723(2)	13.728(1)	
c (Å)	13.722(6)	13.722(1)	
$\alpha = \beta = \gamma$ (º)	90	90.000	
V (Å^3)	2,584.315(7)	2,586.02(42)	
χ_r	71.02(0.54)		
$\boldsymbol{D_{hkl}}$(nm)	43		
Pitiglianoite			
a = *b* (Å)	22.067(1)		22.121(3)
c (Å)	5.214(3)		5.221(1)
$\alpha = \beta$ (º)	90		90.000
γ (º)	120		120.000
V (Å^3)	2,198.955(3)		2,212.55(73)
χ_r	28.98(0.47)		
$\boldsymbol{D_{hkl}}$(nm)	37		
R_Factors: R_p = 19.6; R_{wp} = 23.8; R_{exp} = 12.84; χ^2 = 3.44 and GoF = 1.85.			

In addition, the unit cells of the crystalline structures of the Analcime and Pitiglianoite zeolites are shown in parts of Figure 8(a-b). These structures were modeled using the crystallographic information obtained from the structural refinement, employing the VESTA software. In Figure 8(a), it is possible to observe that the unit cell of the Analcime zeolite contains [MO_4] clusters, where M = Si or Al, both exhibiting tetrahedral symmetry. In addition, distorted octahedral [NaO_6] clusters are present.

On the other hand, Figure 8(b) visually displays the three-dimensional conformation of the unit cell of the Pitiglianoite zeolite, featuring distorted deltahedral [NaO_8] and [KO_8] clusters, as well as tetrahedral [MO_4] clusters, where M = Si or Al. The presence of cations with relatively large ionic radii, such as sodium and potassium, as observed in the obtained structures, may be a promising characteristic for applications in ion exchange or heavy metal adsorption, since their electronic and structural features are favorable for such purposes.

Figure 8

(a) Schematic representation of the unit cell of Analcime zeolite and (b) Pitiglianoite zeolite.

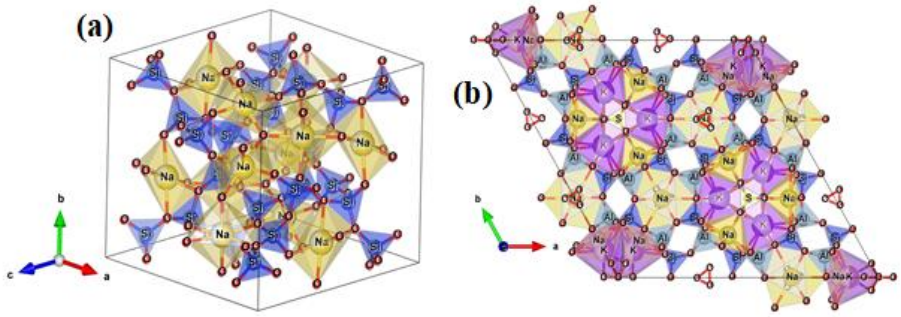

In the study conducted by de León Ramirez *et al.*, (2024) during the synthesis of LTA zeolite, also known as NaA zeolite, the authors performed cationic substitution with zinc ions and investigated the antimicrobial properties of the resulting material. Their results confirmed improved performance against *Escherichia coli* (E. coli) and *Enterococcus faecalis* (E. faecalis) strains compared with the pure zeolite. In another study, Sun *et al.*, (2022) investigated the polychromatic properties of pure and silver-doped LTA zeolite produced via ion exchange. Their findings showed that $Ag_4(H_2O)_n^{2+}$ clusters effectively contribute to color emission in the wavelength range from orange to violet. Similarly, Ferreira *et al.*, (2016) reported the doping of NaY zeolite with zinc and silver ions, confirming that these substituted ions do not occupy specific positions within the zeolite framework but are most likely replacing sodium ions and forming reduced species and water-complexed clusters on the surface of the structures.

The textural properties of the synthesized zeolite were investigated by N_2 adsorption/desorption, as shown by the hysteresis loop in Figure 9. According to IUPAC classification and the consulted literature (FERNANDES *et al.*, 2024) , the profile presented in Figure 9 can be classified as a type IV isotherm, which is characteristic of mesoporous materials, i.e., materials with average pore diameters between 2 and 50 nm. This observation indicates that the crystalline phases forming the mixture do not exhibit a predominance of micropores but instead present an intermediate porous network, consistent with the crystallite sizes previously determined by X-ray diffraction and Rietveld refinement. The specific surface area, determined using Brunauer–Emmett–Teller (BET) analysis, was 11.433 $m^2 \cdot g^{-1}$, a value in close agreement with data reported in the literature, which place the specific surface area of Analcime zeolite, both natural and synthetic, between 8 and 14 $m^2 \cdot g^{-1}$ (YUAN *et al.*, 2016).

Figure 9

N_2 adsorption/desorption hysteresis loop for the synthesized zeolite.

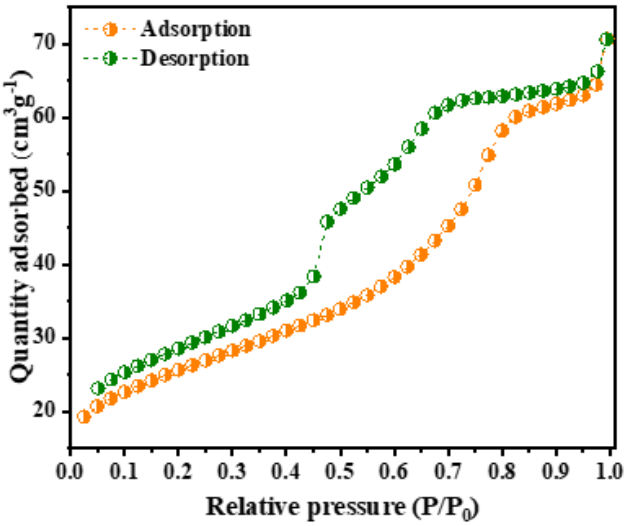

The morphological characterization obtained by scanning electron microscopy (SEM), combined with EDS (energy-dispersive X-ray spectroscopy) analysis and interpretation of the structural formation mechanisms, is illustrated in Figures 10(a–c). The observation of Figure 10(a) shows that the sample is predominantly composed of microcrystals with an almost spherical geometry, although many display surface imperfections such as roughness, cavities, and smaller secondary particles adhered to the main crystal surface. These morphological aspects are consistent with patterns described in the literature, which report the occurrence of such irregularities in crystalline materials produced by hydrothermal synthesis (YUAN *et al.*, 2016). This morphology is characteristic of Analcime zeolite, in which faceted structures with spherical organization are formed, directly influenced by synthesis conditions, the presence of surfactants, and/or the types of precursors used (FERNANDES *et al.*, 2024).

Thus, it is inferred that the elongated microcrystals, rod-like structures with dimensions ranging from 0.3 to 4.3 μm, although observed in lower proportion in the micrograph, are possibly associated with the crystalline phase of Pitiglianoite zeolite, whose framework tends to generate this typical elongated morphology. The EDX spectrum of the zeolite, shown in Figure 10(b), exhibits all dispersive energy peaks associated with the elements expected in the zeolitic matrix, namely sodium (Na), silicon, aluminum, and oxygen. These are evidenced at their respective energies of 1.04 keV, 1.74 keV, 1.48 keV, and 0.52 keV.

Figure 10

(a) scanning electron microscopy (SEM) image, (b) EDX spectrum, and (c) proposed mechanism for the formation of the crystalline phases of the synthesized zeolite.

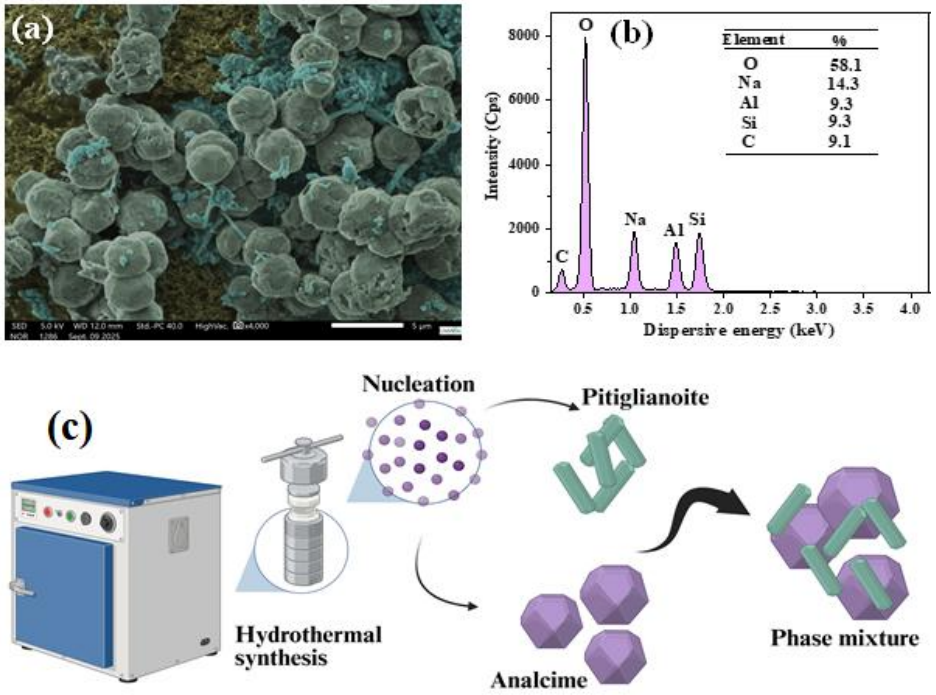

The energy peak corresponding to carbon observed in the EDX spectrum is related to the carbon tape used to fix the sample onto the metallic stub, which serves as the support during SEM analysis. Additionally, the elemental composition of the zeolitic matrix showed approximate proportions of 58.1% oxygen (O), 14.3% sodium (Na), 9.3% aluminum (Al), and 9.3% silicon (Si), values consistent with the typical stoichiometry of zeolitic structures.

Based on the experimental evidence obtained, a schematic representation of the formation process of the Analcime and Pitiglianoite zeolite microcrystals was developed, as illustrated in Figure 10(c). During hydrothermal treatment, the elevated temperature and pressure conditions, combined with the strongly alkaline medium, promoted nucleation and growth of the [AlO_4] and [SiO_4] structural units, which self-assembled via electrostatic interactions and the surface energy of each system. This process resulted in the formation of spherical crystals for the Analcime phase, while Pitiglianoite evolved into elongated rod-like structures, confirming the coexistence of crystalline phases observed in the structural analyses previously discussed.

The evaluation of the heavy metal adsorption capacity of the zeolite was conducted using solutions of different concentrations of lead ions (Pb^{2+}), employing atomic absorption spectroscopy (AAS) as the analytical technique, as shown in Figures 11(a–b). Initially, a calibration curve was constructed from standard Pb^{2+} solutions at concentrations of 0.25,

0.50, 0.75, 1.0, and 1.5 ppm, correlating absorbance with concentration, as illustrated in Figure 11(a). The linear fit of the experimental data resulted in the equation $y = 1.086 \times 10^{-3} + 2.375 \times 10^{-2}x$, with a coefficient of determination $r^2 = 0.9546$, indicating good correlation between absorbance and concentration.

Based on this calibration curve, the percentage of Pb^{2+} removal by the zeolite after 1 hour of contact was determined for the various concentrations tested, as shown in Figure 11(b). The analysis indicates that the average absorbance increased proportionally with the initial concentration of the pollutant ion, confirming an almost linear adsorption behavior and showing no signs of lead resolubilization in the reaction medium during the experiment.

Figure 11

(a) Calibration curve for Pb^{2+} solutions in the 0.25–1.5 ppm range, and (b) absorbance results for solutions with initial concentrations of 10, 20, 50, 80, and 100 ppm and the corresponding percentage removal obtained in the adsorption assays.

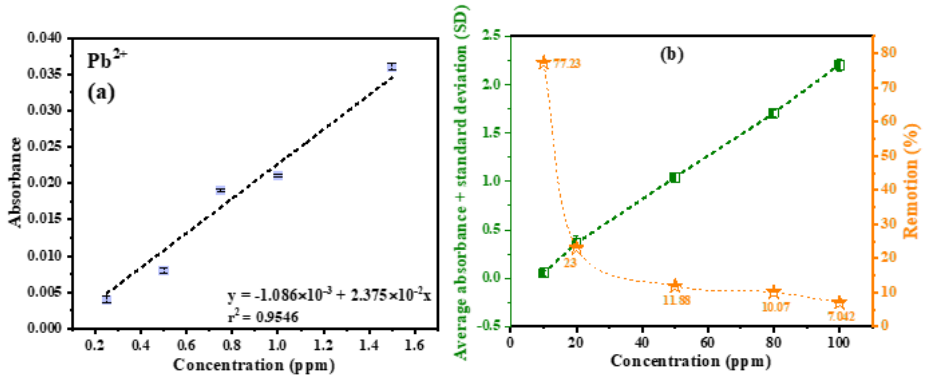

The adsorption percentage was calculated using Equation 3, where C_0 is the initial concentration and C_e is the equilibrium concentration.

$$\%\, remove = \frac{(C_0 - C_e)}{C_0} \times 100 \qquad (3)$$

It was observed that the zeolite exhibited significant efficiency in the removal of Pb^{2+} ions, achieving approximately 77.23% removal when the initial solution concentration was 10 ppm. As the initial lead concentration increased, the adsorptive capacity of the zeolite decreased exponentially, resulting in removal percentages of 23.00%, 11.88%, 10.07%, and 7.04% for initial concentrations of 20, 50, 80, and 100 ppm, respectively. These results highlight the influence of surface saturation on the adsorbent's performance.

The adsorptive capacity of the zeolite under the experimental conditions was calculated using the mathematical formalism presented in Equation 4 (HONG et al., 2019).

In this equation, C_0 corresponds to the initial concentration, C_e to the equilibrium concentration, measured here after 1 hour of contact, V is the volume of solution in liters, and m is the mass of zeolite used in the experiment (0.010 g). Accordingly, the adsorption capacities were 77.23 mg·g^{-1}, 46.00 mg·g^{-1}, 59.40 mg·g^{-1}, 80.53 mg·g^{-1}, and 70.42 mg·g^{-1} for the experiments conducted with initial Pb^{2+} concentrations of 10, 20, 50, 80, and 100 mg·L^{-1}, respectively.

$$q_e = \frac{(C_0 - C_e) \times V}{m} \quad (4)$$

In the study conducted by Kuldeyev *et al.*, (2023) natural Clinoptilolite zeolite collected from the Shankanay mineral deposit in Almaty, Kazakhstan, was subjected to different thermal treatment temperatures for 2 hours and subsequently used in adsorption experiments under several conditions for the remediation of cadmium, lead, nickel, and copper. The authors reported adsorption percentages of 78%, 98%, 83%, and 88% for nickel, copper, cadmium, and lead, respectively. In another study, Hong *et al.*, (2019) synthesized LTA and Faujasite zeolites using the hydrothermal method at 100 °C and used the resulting materials in the adsorption of copper and lead ions in aqueous media, obtaining adsorption capacities of approximately 170 mg·g^{-1} and 510 mg·g^{-1}, respectively. The authors highlight that among the favorable characteristics for the adsorption process, surface charge, ion-exchange capacity, the presence of hydroxyl groups, and the crystallinity of the zeolites were the main factors contributing to the observed performance.

In the study reported by Salek Gilani *et al*. (2024) the adsorptive capacity of Analcime zeolite for the remediation of lead-containing solutions was evaluated, resulting in an adsorption capacity of 54.64 mg·g^{-1}. The best performance was achieved at pH 6, using a catalyst dosage of 4 mg and a contact time of 30 minutes, yielding 95% removal. Based on the results obtained in the present work, it can be inferred that the phase mixture of Analcime and Pitiglianoite zeolites synthesized here exhibited a synergistic effect, enhancing the adsorptive capacity of Analcime when compared with the results reported in the literature for pure Analcime, as previously described. This improved performance may be attributed to structural and textural factors related to the phase mixture, such as increased specific surface area, the presence of crystalline defects, and interfacial effects between microcrystals. These features promote oxygen vacancies, different metal valence states within the clusters, and a heterogeneous distribution of hydroxyl groups across the surface, all of which contribute to stronger interactions with metal ions in solution.

4 CONCLUSION

The results confirm the efficiency of obtaining biogenic silica from the Amazonian Cauxi, displaying a predominantly amorphous pattern with residual quartz. Elemental characterization indicated silicon as the major component (82.43%), along with traces of aluminum (7.17%), phosphorus (0.76%), sulfur (0.72%), potassium (0.34%), calcium (0.46%), and titanium (0.062%). Metakaolinite was produced by the thermal decomposition of kaolinite at 700 °C for 4 hours, as confirmed by X-ray diffraction and infrared spectroscopy. The typical crystallographic planes of kaolinite disappeared, giving rise to an amorphous pattern with residual peaks of quartz and anatase.

The hydrothermal synthesis of the zeolites produced a multiphase mixture composed of Analcime (cubic, Ia-3d) and Pitiglianoite (hexagonal, $P6_3$), with crystallite sizes of 43 nm and 37 nm, respectively. Electron microscopy revealed spherical, porous microcrystals typical of Analcime and elongated rod-like crystals associated with Pitiglianoite. Elemental analysis confirmed the presence of O, Na, Si, and Al, consistent with the expected composition.

The N_2 adsorption profile classified the material as mesoporous, with a specific surface area of 11.433 $m^2 \cdot g^{-1}$ (BET). Lead-removal tests in aqueous solution demonstrated high efficiency, with a maximum adsorption capacity of 77.23 $mg \cdot g^{-1}$, exceeding values reported in the literature. These results show that using biogenic silica and alternative aluminum sources enables the production of multiphase zeolites with suitable physicochemical properties, offering a promising strategy for developing materials aimed at the remediation of heavy metals in aqueous media.

ACKNOWLEDGMENTS

The authors thank the Coordination for the Improvement of Higher Education Personnel (CAPES) and the Amazonas State Research Support Foundation (FAPEAM) for the financial support provided for the acquisition of supplies necessary for the full development of the project's activities.

REFERENCES

ABDELHALIM, A.; MELEGY, A.; OTHMAN, D. Assessment of synthetic zeolites from kaolin and bentonite clays for wastewater and fuel gases treatment. Journal of African Earth Sciences, v. 227, n. August 2024, p. 105621, jul. 2025. Disponível em: <https://linkinghub.elsevier.com/retrieve/pii/S1464343X25000883>.

AFZAL, I. et al. Comparative analysis of heavy metals toxicity in drinking water of selected industrial zones in Gujranwala, Pakistan. Scientific Reports, v. 14, n. 1, p. 1–21, 2024.

ALBUQUERQUE, A. R. et al. Theoretical Study of the Stoichiometric and Reduced Ce-Doped TiO 2 Anatase (001) Surfaces. The Journal of Physical Chemistry C, v. 119, n. 9, p. 4805–4816, 5 mar. 2015. Disponível em: <https://pubs.acs.org/doi/10.1021/jp5105483>.

ANDRADES, R. C. et al. Influence of Alkalinity on the Synthesis of Zeolite A and Hydroxysodalite from Metakaolin. Journal of Nano Research, v. 61, p. 51–60, 12 fev. 2020. Disponível em: <https://www.scientific.net/JNanoR.61.51>.

ARAUJO, E. C. G. et al. Bioeconomy in the Amazon: Lessons and gaps from thirty years of non-timber forest products research. Journal of Environmental Management, v. 370, n. August, p. 122420, nov. 2024. Disponível em: <https://linkinghub.elsevier.com/retrieve/pii/S030147972402406X>.

BARROS, I. B. et al. Elemental Composition of Freshwater Sponge Metania fittkaui Volkmer-Ribeiro. Revista Virtual de Química, v. 6, n. 5, p. 1380–1390, 2014. Disponível em: <https://rvq.sbq.org.br/audiencia_pdf.asp?aid2=238&nomeArquivo=v6n5a17.pdf>.

CECILIA, J. A. et al. Kaolinite-based zeolites synthesis and their application in CO2 capture processes. Fuel, v. 320, n. December 2021, 2022.

CHAKRABORTY, A. K. Phase Transformation of Kaolinite Clay. 1. ed. New Delhi: Springer India, 2014. Disponível em: <https://link.springer.com/10.1007/978-81-322-1154-9>.

CHENG, H.; ZHOU, Y.; LIU, Q. 6 - Kaolinite Nanomaterials: Preparation, Properties and Functional Applications. In: WANG, A.; WANG, W. B. T.-N. FROM C. M. (Org.). . Micro and Nano Technologies. [S.l.]: Elsevier, 2019. p. 285–334. Disponível em: <https://www.sciencedirect.com/science/article/pii/B9780128145333000065>.

DE BARROS, I. B. Elemental Composition of Drulia browni Collected in Negro River (Amazonas, Brazil). Journal of Analytical & Bioanalytical Techniques, v. S6, n. 002, p. 10–13, 2014. Disponível em: <https://www.omicsonline.org/open-access/elemental-composition-of-drulia-browni-collected-in-negro-river-2155-9872.S12-011.php?aid=26126>.

DE LEÓN RAMIREZ, J. I. et al. Antimicrobial activity of the LTA zeolite modified by zinc species. Microporous and Mesoporous Materials, v. 380, n. August, 2024.

DE S. BARROS, S. et al. Pineapple (Ananás comosus) leaves ash as a solid base catalyst for biodiesel synthesis. Bioresource Technology, v. 312, n. May, 2020.

EL-SAYED, K.; HEIBA, Z. K.; ABDEL-RAHMAN, A. M. Crystal structure analysis and refinement of Kalabsha kaolinite (Al 2 Si 2 O 5 (OH) 4). Crystal Research and Technology, v. 25, n. 3, p. 305–312, 5 mar. 1990. Disponível em: <https://onlinelibrary.wiley.com/doi/10.1002/crat.2170250314>.

FERNANDES, L. et al. Synthesis of Analcime Zeolite from Glass Powder Waste and Aluminium Anodizing Waste. Silicon, n. 0123456789, 2024. Disponível em: <https://doi.org/10.1007/s12633-024-02992-z>.

FERREIRA, L. et al. Microbial growth inhibition caused by Zn/Ag-Y zeolite materials with different amounts of silver. Colloids and Surfaces B: Biointerfaces, v. 142, p. 141–147, 2016. Disponível em: <http://dx.doi.org/10.1016/j.colsurfb.2016.02.042>.

GAO, L. et al. Heliyon Effect of phosphoric acid content on the microstructure and compressive strength of phosphoric acid-based metakaolin geopolymers. HLY, v. 6, n. 4, p. e03853, 2020. Disponível em: <http://dx.doi.org/10.1016/j.heliyon.2020.e03853>.

GUZMÁN-APONTE, L. A.; DE GUTIÉRREZ, R. M.; MAURY-RAMÍREZ, A. Metakaolin-based geopolymer with added TiO 2 particles: Physicomechanical characteristics. Coatings, v. 7, n. 12, p. 1–12, 2017.

HONG, M. et al. Heavy metal adsorption with zeolites: The role of hierarchical pore architecture. Chemical Engineering Journal, v. 359, n. August 2018, p. 363–372, 2019. Disponível em: <https://doi.org/10.1016/j.cej.2018.11.087>.

HSIEH, Y.-L.; YEH, S.-C. The trends of major issues connecting climate change and the sustainable development goals. Discover Sustainability, v. 5, n. 1, p. 31, 12 mar. 2024. Disponível em: <https://doi.org/10.1007/s43621-024-00183-9>.

IZABELITA S. LACERDA, D.; C. COUCEIRO, P. R. MCM-41 Derived from Freshwater Sponge Silica as Support for HPW Applied in the Esterification of Oleic Acid. Revista Virtual de Química, v. 11, n. 4, p. 1106–1121, 2019. Disponível em: <http://rvq.sbq.org.br/audiencia_pdf.asp?aid2=1080&nomeArquivo=v11n4a04.pdf>.

JOMOVA, K. et al. Heavy metals: toxicity and human health effects. [S.l: s.n.], 2025. v. 99.

JORGENSEN, J. D. Compression mechanisms in α-quartz structures - SiO2 and GeO2. Journal of Applied Physics, v. 49, n. 11, p. 5473–5478, 1978.

KHALEQUE, A. et al. Zeolite synthesis from low-cost materials and environmental applications: A review. Environmental Advances, v. 2, n. October, 2020.

KHELIFI, F. et al. Bioaccessibility of potentially toxic metals in soil, sediments and tailings from a north Africa phosphate-mining area: Insight into human health risk assessment. Journal of Environmental Management, v. 279, n. November 2020, 2021.

KULDEYEV, E. et al. Modifying Natural Zeolites to Improve Heavy Metal Adsorption. Water, v. 15, n. 12, p. 2215, 12 jun. 2023. Disponível em: <https://www.mdpi.com/2073-4441/15/12/2215>.

KYRIAKOGONA, K.; GIANNOPOULOU, I.; PANIAS, D. Extraction of Aluminium from Kaolin : a Comparative Study of Hydrometallurgical Processes. n. Table 1, p. 2–7, 2017.

LIU, M. et al. Luminescent properties of ZSM-5 zeolite phosphor and its application to aquatic plant lighting and white LEDs. Ceramics International, v. 50, n. 6, p. 9125–9131, mar. 2024. Disponível em: <https://linkinghub.elsevier.com/retrieve/pii/S0272884223041603>.

MALLETTE, A. J. et al. Highly efficient synthesis of zeolite chabazite using cooperative hydration-mismatched inorganic structure-directing agents. Chemical Science, v. 15, n. 2, p. 573–583, 2024. Disponível em: <https://xlink.rsc.org/?DOI=D3SC05625B>.

MARIA, S. Use of Brazilian Kaolin as a Potential Low-cost Adsorbent for the Removal of Malachite Green from Colored Effluents. v. 20, p. 14–22, 2020.

MARUOKA, L. M. A. et al. Effect of thermal annealing on kaolin from the Amazon region, aiming at the production of geopolymer. Journal of Materials Research and Technology, v. 25, p. 2471–2485, 2023a. Disponível em: <https://doi.org/10.1016/j.jmrt.2023.06.105>.

MARUOKA, L. M. A. et al. Effect of thermal annealing on kaolin from the Amazon region, aiming at the production of geopolymer. Journal of Materials Research and Technology, v. 25, p. 2471–2485, jul. 2023b. Disponível em: <https://doi.org/10.1016/j.jmrt.2023.06.105>.

MERLINO, S. et al. Pitiglianoite, a new feldspathoid from southern Tuscany, Italy: chemical composition and crystal structure. American Mineralogist, v. 76, n. 11–12, p. 2003–2008, 1991.

MI, G. et al. Formation of CaTiO3 by grinding from mixtures of CaO or Ca(OH)2 with anatase or rutile at room temperature. Powder Technology, v. 97, n. 2, p. 178–182, jun. 1998. Disponível em: <https://linkinghub.elsevier.com/retrieve/pii/S0032591098000126>.

MICHELANGELI, M. et al. Predicting the impacts of chemical pollutants on animal groups. Trends in Ecology and Evolution, v. 37, n. 9, p. 789–802, 2022.

MORAES, C. G. et al. Produção de zeólita analcima a partir de aculim amazônico. Cerâmica, v. 59, n. 352, p. 563–569, dez. 2013. Disponível em: <http://www.scielo.br/scielo.php?script=sci_arttext&pid=S0366-69132013000400012&lng=pt&tlng=pt>.

NOBRE, F.X. et al. Fast and efficient green synthesis of CaWO4 NPs using eggshells as a biogenic calcium source: Structure, optical property, and morphology. Journal of Photochemistry and Photobiology A: Chemistry, v. 439, n. September 2022, p. 114589, maio 2023. Disponível em: <https://doi.org/10.1016/j.jphotochem.2023.114589>.

NOBRE, FRANCISCO XAVIER et al. Facile synthesis of nTiO2 phase mixture: Characterization and catalytic performance. Materials Research Bulletin, v. 109, n. June 2018, p. 60–71, jan. 2019. Disponível em: <https://linkinghub.elsevier.com/retrieve/pii/S002554081831849X>.

OUYANG, R.; LIU, J.; LI, W. Atomistic Theory of Ostwald Ripening and Disintegration of Supported Metal Particles under Reaction Conditions. Journal of the American Chemical Society, v. 135, n. 5, p. 1760–1771, 6 fev. 2013. Disponível em: <https://pubs.acs.org/doi/10.1021/ja3087054>.

PALA-ROSAS, I. et al. Effects of the Acidic and Textural Properties of Y-Type Zeolites on the Synthesis of Pyridine and 3-Picoline from Acrolein and Ammonia. Catalysts, v. 13, n. 4, 2023.

PAVAN, C. et al. Nearly free silanols drive the interaction of crystalline silica polymorphs with membranes: Implications for mineral toxicity. Frontiers in Chemistry, v. 10, n. January, p. 1–12, 2023.

PÉREZ-BOTELLA, E.; VALENCIA, S.; REY, F. Zeolites in Adsorption Processes: State of the Art and Future Prospects. Chemical Reviews, v. 122, n. 24, p. 17647–17695, 28 dez. 2022. Disponível em: <https://pubs.acs.org/doi/10.1021/acs.chemrev.2c00140>.

PRUETT, R. J. Kaolin deposits and their uses: Northern Brazil and Georgia, USA. Applied Clay Science, v. 131, p. 3–13, out. 2016. Disponível em: <https://linkinghub.elsevier.com/retrieve/pii/S0169131716300515>.

QI, G. et al. Synergic Effect of Active Sites in Zinc-Modified ZSM-5 Zeolites as Revealed by High-Field Solid-State NMR Spectroscopy. Angewandte Chemie International Edition, v. 55, n. 51, p. 15826–15830, 19 dez. 2016. Disponível em: <https://onlinelibrary.wiley.com/doi/10.1002/anie.201608322>.

RAMAN, R. et al. The impact of Gen Z's pro-environmental behavior on sustainable development goals through tree planting. Sustainable Futures, v. 8, n. March, 2024.

RHODES, C. J. Properties and applications of Zeolites. Science Progress, v. 93, n. 3, p. 223–284, 1 ago. 2010. Disponível em: <https://journals.sagepub.com/doi/10.3184/003685010X12800828155007>.

SALEK GILANI, N.; EHSANI TILAMI, S.; AZIZI, S. N. Synthesized analcime zeolite: an effective adsorbent for removal of Pb(II) ions from aqueous solution. Inorganic and Nano-Metal Chemistry, v. 54, n. 8, p. 804–812, 2 ago. 2024. Disponível em: <https://doi.org/10.1080/24701556.2022.2078350>.

SARAVANAN, P. et al. Comprehensive review on toxic heavy metals in the aquatic system: sources, identification, treatment strategies, and health risk assessment. Environmental Research, v. 258, n. November 2023, 2024.

SILVA FILHO, S. H. DA et al. Synthesis of Zeolite A employing Amazon kaolin waste. Cerâmica, v. 61, n. 360, p. 409–413, dez. 2015. Disponível em: <http://www.scielo.br/scielo.php?script=sci_arttext&pid=S0366-69132015000400409&lng=en&tlng=en>.

SOARES, I. et al. Study of Metakaolinite Geopolymeric Mortar with Plastic Waste Replacing the Sand: Effects on the Mechanical Properties, Microstructure, and Efflorescence. Materials, v. 15, n. 23, p. 8626, 2 dez. 2022. Disponível em: <https://www.mdpi.com/1996-1944/15/23/8626>.

SOUSA, C. DO V. M. DE et al. Rediscovery after three decades of the freshwater sponge Metania kiliani on a terrestrial fern. Acta Amazonica, v. 55, 2025. Disponível em: <http://www.scielo.br/scielo.php?script=sci_arttext&pid=S0044-59672025000101205&tlng=en>.

SULTHANA, S. F. et al. Electrochemical Sensors for Heavy Metal Ion Detection in Aqueous Medium: A Systematic Review. ACS Omega, v. 9, n. 24, p. 25493–25512, 2024.

SUN, L. et al. Origin of the polychromatic photoluminescence of zeolite confined Ag clusters: temperature- and co-cation-dependent luminescence. Chemical Science, v. 13, n. 39, p. 11560–11569, 2022.

TOBY, B. H. R factors in Rietveld analysis: How good is good enough? Powder Diffraction, v. 21, n. 1, p. 67–70, 1 mar. 2006. Disponível em: <https://www.cambridge.org/core/product/identifier/S0885715600003250/type/journal_article>.

VELARDE, L. et al. Adsorption of heavy metals on natural zeolites: A review. Chemosphere, v. 328, n. March, p. 138508, jul. 2023. Disponível em: <https://linkinghub.elsevier.com/retrieve/pii/S0045653523007750>.

WANG, J. et al. Pseudocapacitive contributions to electrochemical energy storage in TiO 2 (anatase) nanoparticles. Journal of Physical Chemistry C, v. 111, n. 40, p. 14925–14931, 2007.

XU, L. et al. A Review on Remediation Technology and the Remediation Evaluation of Heavy Metal-Contaminated Soils. Toxics, v. 12, n. 12, p. 897, 10 dez. 2024. Disponível em: <https://www.mdpi.com/2305-6304/12/12/897>.

YUAN, J. et al. Crystal structural transformation and kinetics of <math altimg="si1.gif" overflow="scroll"> <mrow> <msup> <mrow> <msub> <mrow> <mtext>NH</mtext> </mrow> <mn>4</mn> </msub> </mrow> <mo>+</mo> </msup> </mrow> </math> /Na+ ion-exchange in analcime. Microporous and Mesoporous Materials, v. 222, n. 3, p. 202–208, mar. 2016. Disponível em: <http://dx.doi.org/10.1016/j.micromeso.2015.10.020>.

ZUO, K. et al. Structural transformation and dehydroxylation of clay minerals in lithium-bearing clay. Journal of Thermal Analysis and Calorimetry, v. 147, n. 23, p. 13231–13237, 29 dez. 2022. Disponível em: <https://doi.org/10.1007/s10973-022-11581-4>.